UC Santa Barbara
UC Santa Barbara Previously Published Works

Title

Impact of Mg Substitution on the Structure, Stability, and Properties of the Na2Fe2F7 Weberite Cathode

Permalink

Authors

Porter, Hanna Z
Foley, Emily E
Jin, Wen
et al.

Publication Date

DOI

Copyright Information

Peer reviewed

Impact of Mg substitution on the structure, stability, and properties of the $Na_2Fe_2F_7$ weberite cathode

Hanna Z. Porter,[1,2] Emily E. Foley,[1,2] Wen Jin,[1,2] Eric Chen,[1,2] Erick A. Lawrence,[1,2] Euan N. Bassey,[1,2] Raphaële J. Clément*[1,2]

[1]Materials Department, University of California Santa Barbara, California 93106, USA

[2]Materials Research Laboratory, University of California Santa Barbara, California 93106, USA

Email: rclement@ucsb.edu

Abstract

Of the few weberite-type Na-ion cathodes explored to date, $Na_2Fe_2F_7$ exhibits the best performance, with capacities up to 184 mAh/g and energy densities up to 550 Wh/kg reported for this material. However, the development of robust structure-property relationships for this material is complicated by its tendency to form as a mixture of metastable polymorphs, and transform to a lower-energy Na_yFeF_3 perovskite compound during electrochemical cycling. Our first principles-guided exploration of Fe-based weberite solid solutions with redox-inactive Mg^{2+} and Al^{3+} predicts an enhanced thermodynamic stability of $Na_2Mg_xFe_{2-x}F_7$ as the Mg content is increased, and the $x = 0.125$ composition is selected for further exploration. We demonstrate that the monoclinic polymorph (space group $C2/c$) of $Na_2Fe_2F_7$ (Mg0) and of a new Mg-substituted weberite composition, $Na_2Mg_{0.125}Fe_{1.875}F_7$ (Mg0.125), can be isolated using an optimized synthesis protocol. The impact of Mg substitution on the stability of the weberite phase during electrochemical cycling, and on the extent and rate of Na (de)intercalation, is examined. Irrespective of the Mg content, we find that the weberite phase is retained when cycling over a narrow voltage window (2.8–4.0 V vs. Na/Na^+). Over a wider voltage range (1.9–4.0 V), Mg0 shows steady capacity fade due to its transformation to the Na_yFeF_3 perovskite phase, while Mg0.125 displays more reversible cycling and a reduced phase transformation. Yet, Mg incorporation also leads to kinetically limited Na extraction, and a reduced overall capacity. These findings highlight the need for the continued compositional optimization of weberite cathodes to improve their structural stability while maximizing their energy density.

Keywords:

Sodium-ion Batteries, Structure Stabilization, Materials Design, Transition Metal Fluorides, Weberite

Introduction

Rechargeable batteries have become a central component of modern life, powering devices and enabling the transition to carbon-free energy sources through the electrification of transportation and grid-scale energy storage systems. While lithium-ion batteries (LIBs) have largely formed the basis for such applications,[1–5] growing concerns about the availability, cost, and geographic concentration of elements critical for the cathodes in these systems, namely lithium (Li), nickel (Ni), and cobalt (Co),[6–9] have motivated the development of sustainable and cost-effective alternative chemistries with energy densities on par with those offered by LIBs.

Sodium ion batteries (SIBs) are the most developed 'beyond lithium' battery technology, and benefit from the higher natural abundance, ease and sustainability of resource extraction, and thus lower cost of sodium (Na) as compared to Li.[8,10] Rapid improvements in the energy density and capacity of SIBs over the past decade have enabled the commercialization of the first generation of SIBs with gravimetric energy densities of up to 160 Wh/kg (approaching the energy density of industry-standard $LiFePO_4$-based cells),[11,12] with applications in grid-scale energy storage,[13,14] moderate-range electric vehicles,[15,16] and as replacements for lead-acid batteries.[11] Yet, the capacity and energy density of SIBs still lags behind that of state-of-the-art Li cells powered by $LiNi_{0.8}Mn_{0.1}Co_{0.1}O_2$ (NMC811) or $LiNi_{0.8}Co_{0.15}Al_{0.05}O_2$ (NCA) cathodes. The development of energy-dense and high-powered SIBs hinges largely on improving the performance of the cathode material. Further, the replacement of expensive and environmentally- and ethically-fraught elements, such as Ni and Co, by earth abundant transition metals, such as iron (Fe) and manganese (Mn), in the cathode material is key to further reducing the cost and environmental impact of SIBs. Layered $NaMO_2$ (M = Fe, Mn) cathodes[17–20] have demonstrated high capacities and energy densities but suffer from capacity fade related to partially irreversible layer glide phase transitions,[17,18,21] with further structural degradation stemming from transition metal migration,[22,23] strain-inducing Jahn-Teller distortions,[24,25] transition metal dissolution, and oxygen loss.[26] In contrast, Fe- and Mn-based polyanionic compounds ($NaMPO_4$, $Na_2MP_2O_7$, $Na_2M(SO_4)_3$ M = Fe, Mn) exhibit excellent structural stability from the presence of strong covalent P-O and S-O bonds, resulting in good cycling stability, but low energy densities due to the bulky and heavy polyanions.[27–31] Clearly, further work is needed to identify a Na-ion cathode material satisfying all of the performance, sustainability, and cost criteria mentioned above.

A potential strategy for improving the energy density of SIBs is through bulk fluorine (F) incorporation; as the most electronegative element, incorporation of F acts to raise the operating potential of the cathode *via* the inductive effect.[32–35] While polyanions can also lead to a strong inductive effect, and thus high potentials, the significantly lower molecular weight of F is advantageous with regard to the specific capacity and gravimetric energy density. While F has been previously incorporated into oxide-[33,36,37] and polyanion-based cathodes,[35,38–40] few pure fluorides have been identified as intercalation-type cathodes. In fact, the limited electronic and ionic conductivity of fluoride compounds often results in conversion reactions during electrochemical cycling,[41–43] with poor reversibility, and/or sluggish reaction kinetics.[32,44] Poor electronic conduction can be alleviated by the addition of conductive carbons (either by carbon-coating or mixing-based methods), particle downsizing, and electrode nanostructuring.[45–47] Further, to promote reversible and structure-preserving Na (de)intercalation processes, open-framework fluoride structures with fast Na-transport pathways must be identified.

Recently, weberite-type sodium metal fluorides have emerged as potential Na-ion intercalation cathodes. The weberite structure, with general formula $A_2B_2X_7$, can be described as an anion-deficient fluorite. The anion deficiency results in a decrease in the coordination number of the B cations, from 8-coordinate in a regular fluorite to 6-coordinate, greatly expanding the possible range of species occupying those sites, while the A cations remain 8-fold coordinated (**Figure S1**). In the case of weberite Na-ion cathodes with chemical

formula $Na_2M^{2+}M'^{3+}F_7$, at least one of the M and M' species occupying the B sites is redox active. The relatively low-density, open-framework weberite structure, and the presence of three-dimensionally connected Na-ion channels in $Na_2MM'F_7$ compounds, hold promise for facile Na-ion diffusion and topotactic Na-ion (de)intercalation. Assuming the reversible removal and reinsertion of two Na ions per formula unit on charge and discharge, a computational study of $Na_2MM'F_7$ cathodes by Euchner *et al.*[48] predicted theoretical energy densities higher than that of any known Na-ion intercalation cathode (*ca.* 600–800 Wh/kg), and comparable to those of state-of-the-art Li-ion NMC or NCA cathodes. In addition, low activation energy barriers were obtained from first principles, confirming facile Na-ion diffusion through the large and interconnected channels.[48] So far, $Na_2Fe_2F_7$,[49–52] Na_2TiFeF_7,[53] Na_2MVF_7 (M = Mn, Fe, Co),[54] have been tested as Na-ion cathodes.

To date, the weberite cathode with the best performance metrics is $Na_2Fe_2F_7$, for which a range of crystal structures and electrochemical behaviors have been reported.[49,55–57] Orthorhombic *Imma*,[49,55,56] trigonal $P3_121$,[50] and monoclinic $C2/c$[57] crystal structures have been observed, which differ in the stacking of their Kagomé-like close-packed cation layers (**Figure S1**). These polymorphs are referred to as $2O$ (*Imma*), $3T$ ($P3_121$), and $4M$ ($C2/c$) respectively, a nomenclature system that conveys the number of cation slabs per repeating unit (2, 3, or 4), and the symmetry of the structure (*O*, *T*, or *M*). In our recent work, we showed, using first principles calculations, that the $2O$, $3T$, and $4M$ polymorphs are all metastable and within 5 meV/atom from one another for Na_2Fe_2F,[51] and in fact this compound could only be prepared as a mixture of the different polymorphs, with potential implications for the electrochemical performance.[51] We note that most other reports on this cathode mateial[49,50,55–57] have lacked the high-resolution XRD data necessary to provide a detailed account of its polymorphic makeup, complicating the establishment of structure-property relationships.

Regarding the electrochemical performance of $Na_2Fe_2F_7$, Park *et al.* reported a remarkable initial capacity of 184 mAh/g at $C/20$, approaching the theoretical limit assuming the exchange of two Na ions per formula unit, and good rate performance with 77% of the slow-rate capacity retained at $5C$.[50] In full cells, $Na_2Fe_2F_7$ exhibited outstanding cycle stability, maintaining 88.3% of the initial capacity (118 mAh/g) after 1000 cycles at a rate of $2C$.[50] In contrast, other studies, including work by Dey *et al.* and our own, revealed more modest electrochemical performance for this material.[49,51] We found that $Na_2Fe_2F_7$ exhibits an initial reversible capacity of 125 mAh/g when cycled between 1.5 and 4.3 V *vs.* Na/Na$^+$, 60% capacity retention after 50 cycles at $C/20$, and a substantial capacity drop-off at higher than $C/5$ rates.[51] We hypothesized that the discrepancy between the various reports could be due to different electrode formulations and processing strategies, as these parameters have been found to greatly influence the performance of strongly electronically insulating electrodes.[47,51,58–62] Notably, our $Na_xFe_2F_7$ cathode underwent a transformation to a lower-capacity perovskite Na_yFeF_3 phase during electrochemical cycling,[51] which likely accounts for the capacity fade observed in this system together with HF evolution. Clearly, the development of single-phase weberite compounds that are stable over a wide range of Na compositions is necessary to develop more robust structure-property relationships for this class of cathodes and improve their cyclability.

To improve the stability of the weberite $Na_2Fe_2F_7$ cathode in the pristine state, we focus our attention on partial substitution of Fe^{2+} and Fe^{3+} for redox-inactive Mg^{2+} and Al^{3+}, respectively, as the weberite structure can readily accommodate both, as shown by the naturally occurring weberite mineral Na_2MgAlF_7. Selection of promising weberite compositions for the present study was informed by first principles density functional theory (DFT) calculations of the phase stability of the resulting solid solutions. The results, obtained for $Na_2Mg_xFe_{2-x}F_7$ and $Na_2Fe_{2-x}Al_xF_7$ compositions with x = 0.000, 0.125, 0.250, 0.500, 0.750, and 1.000, are presented in **Figures 1 and S2**. To compare the stability of various weberite compositions, decomposition energies were determined by first calculating the energies of all relevant binary or ternary fluoride phases,

enumerating all possible decomposition pathways starting from the relevant weberite composition, using the DFT-obtained energies to calculate the energy of each pathway, and taking the higher reaction energy as the decomposition energy. Here, a positive decomposition energy indicates an unstable or metastable weberite phase, while a negative decomposition energy indicates a thermodynamically stable weberite phase. More details on the computation of the decomposition energy are provided in the methods section and in **Tables S1** and **S2**. Overall, the incorporation of Mg^{2+} stabilizes the weberite structure, with a 20 meV/atom decrease in decomposition energy from $x = 0$ to $x = 1$ (**Figure 1a**), while Al^{3+} incorporation results in a less stable structure with a 40 meV/atom increase in decomposition energy from $x = 0$ to $x = 1$ (**Figure S2b**). This predicted enhanced thermodynamic stability motivates a detailed exploration of Mg incorporation into $Na_2Fe_2F_7$. All Mg-based compositions with $x < 1$ are predicted to be metastable, with a slightly positive decomposition energy (< 20 meV/atom). Nevertheless, we are able to synthesize the entire range of $Na_2Mg_xFe_{2-x}F_7$ compositions, with synchrotron XRD patterns collected on the as-prepared $x = 0.5$ and $x = 1$ compositions shown in **Figure S3** (with refinement details in **Table S3**). Given the need for a high redox-active Fe content for practical Na-ion battery applications, and the predicted enhanced stability upon incorporation of Mg into the structure, we hereafter narrow the focus of our efforts to $Na_2Fe_2F_7$ ($x = 0$) and $Na_2Mg_{0.125}Fe_{1.875}FeF_7$ ($x = 0.125$). The $2O$, $3T$, and $4M$ weberite polymorphs are predicted to be very similar in energy (within 5 meV/atom) for these two weberite compositions (**Figure 1b**), in agreement with our previous results for the all-Fe system.[51]
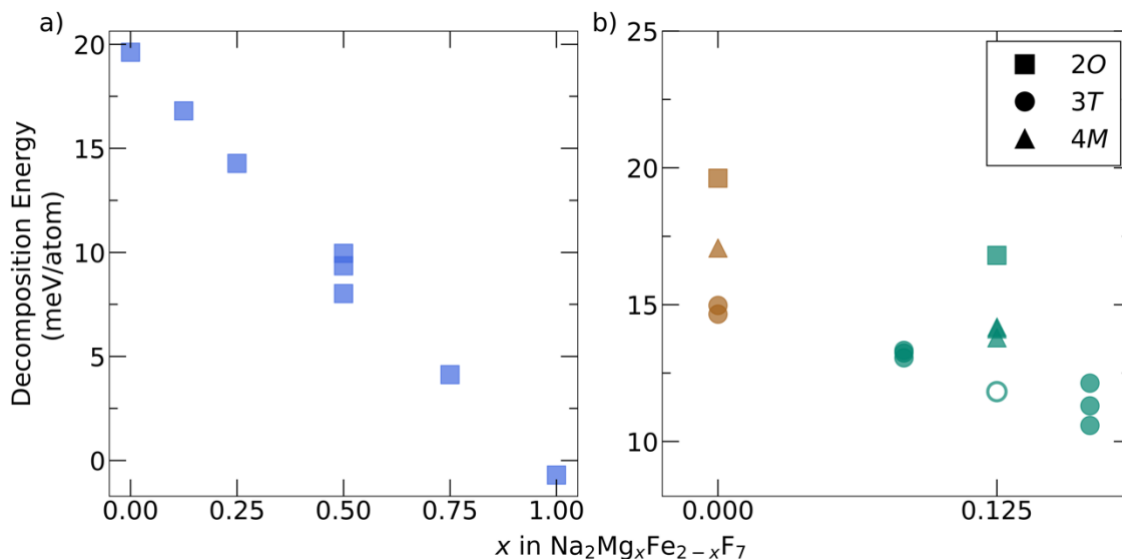
Figure 1. Impact of Mg substitution on the stability of the $Na_2Fe_2F_7$ weberite. *Ab initio* decomposition energies for the most favorable decomposition pathway, $Na_2Mg_xFe_{2-x}F_7 \rightarrow xMgF_2 + (1-x)FeF_2 + 1/2\ NaFeF_4 + 1/2\ Na_3FeF_6$ for (a) the highest symmetry (and least computationally expensive) $2O$ weberite polymorph at $x = 0, 0.125, 0.5, 0.75, 1$, and (b) the $2O$, $3T$, and $4M$ polymorphs at $x = 0.000$ (brown) and $x = 0.125$ (teal). The open circle represents an average value between the lowest energy $3T$ structures at $x = 0.083$ and $x = 0.167$ as the unit cell for the $x = 0.125$ stoichiometry was prohibitively large (216 atoms) for DFT calculations. A positive decomposition energy indicates an unstable or metastable weberite phase, while a negative decomposition energy indicates a thermodynamically stable weberite phase. The r^2SCAN exchange-correlation functional[63] and Hubbard U parameter of 5.4 eV[64] were used throughout, although similar trends in phase stability were obtained using different computational parameters (**Figure S2**).

The goal of the present work is to understand the impact of Mg substitution on the structural and electrochemical properties of the $Na_2Fe_2F_7$ weberite cathode. For this, we compare $Na_2Fe_2F_7$ ($x = 0$) with $Na_2Mg_{0.125}Fe_{1.875}FeF_7$ ($x = 0.125$), hereafter referred to as Mg0 and Mg0.125, respectively. Following optimization of the synthesis conditions, we successfully isolate the $4M$ weberite polymorph for both compositions, as confirmed by synchrotron X-ray diffraction (SXRD) and [23]Na solid-state nuclear magnetic resonance (ss-NMR). Results from electrochemical testing of these cathodes in Na half-cells indicate that the incorporation of Mg into the weberite structure reduces the initial capacity (92 mAh/g for Mg0 *vs.* 72 mAh/g for Mg0.125), but improves the cycling stability over the 1.9–4.0 V voltage range (69% capacity retention for Mg0 *vs.* 82% for Mg0.125 after 50 cycles) by reducing the extent to which the weberite phase transforms to a perovskite phase upon cycling. The phase transformation can be eliminated by limiting the cycling voltage range to 2.8–4.0 V. Despite its improved stability during cycling, Mg0.125 exhibits a significantly lower (22% lower) capacity than Mg0 over the two voltage windows tested here, due to kinetic limitations associated with Na extraction at high voltages.

Results

Structural Characterization of as-prepared and carbon-coated cathode powders

The predicted metastability and polymorphism of weberite $Na_2Fe_2F_7$ (Mg0) and $Na_2Mg_{0.125}Fe_{1.875}FeF_7$ (Mg0.125) compounds (**Figure 1b**) demands careful characterization of the as-prepared and processed (carbon-coated) materials using long-range and local structure probes. We began by studying the effects of the annealing temperature on the phase purity and polymorphic content of the Mg0 and Mg0.125 samples. Both compositions were prepared using an initial mechanochemical milling step (**Figure S4**), then annealing the pelletized product at either 425°C, 500°C, 575°C, or 650°C for 30 minutes, adapting a protocol developed for Mg0.[51] The anneal was followed by a rapid quench. The SXRD patterns obtained on the as-prepared samples are shown in **Figure S5**. Rietveld refinements of the data collected on Mg0 and Mg0.125 samples annealed at 650°C are shown in **Figure 2** (detailed refinement parameters are listed in **Tables S4**–**S6**), while the refinements of the data obtained for samples annealed at the other temperatures are shown in **Figures S6**–**S7.** The refinement results indicate the presence of a single, $4M$ weberite polymorph in all the as-synthesized samples, along with 5–10 wt.% of an Na_3FeF_6 impurity (**Table S7**).

A more detailed analysis of the SXRD data obtained for each annealing temperature provides insight into the formation of the Mg0 and Mg0.125 crystalline structures. The SXRD patterns obtained on samples annealed at 425°C or 500°C exhibit broad peaks, indicating low crystallinity. We note that the quality of the diffraction patterns of the low temperature anneals could potentially obscure the presence of other weberite polymorphs, but a structural model containing a single $4M$ polymorph provides a satisfactory fit of the data, which is not significantly improved upon inclusion of additional weberite phases in the model (**Figures S8**–**9**, **Table S8**). Upon annealing to 575°C, significantly sharper diffraction peaks are observed, with the SXRD pattern obtained on the Mg0.125 sample exhibiting three clear diffraction peaks in the Q range of 2.04–2.12 Å^{-1} corresponding to reflections associated with the (008), (222), and (40$\bar{4}$) planes and characteristic of the $4M$ weberite polymorph. In contrast, those same diffraction peaks are somewhat broadened and overlapping in the SXRD pattern collected on the Mg0 sample annealed at 575°C (**Figure S5**). By 650°C, the SXRD patterns obtained on both Mg0 and Mg0.125, and corresponding Rietveld refinements are consistent with the presence of a single $4M$ weberite polymorph. Refinements of the SXRD patterns collected on the Mg0.125 sample annealed at 650°C where no Mg is included in the structural model or when Mg^{2+} is placed on the Fe^{3+} site yield similar fits to the predicted structural model where Mg^{2+} is incorporated on the Fe^{2+} site (**Figure S10** and **Table S9**). Despite uncertainty about the exact location of

Mg^{2+} within the Mg0.125 structure, the relative shift of the weberite peaks in the SXRD patterns collected on Mg0 and Mg0.125 arise from differences in lattice parameters for these compositions (**Figure S11**), suggesting successful incorporation of Mg into the weberite structure.
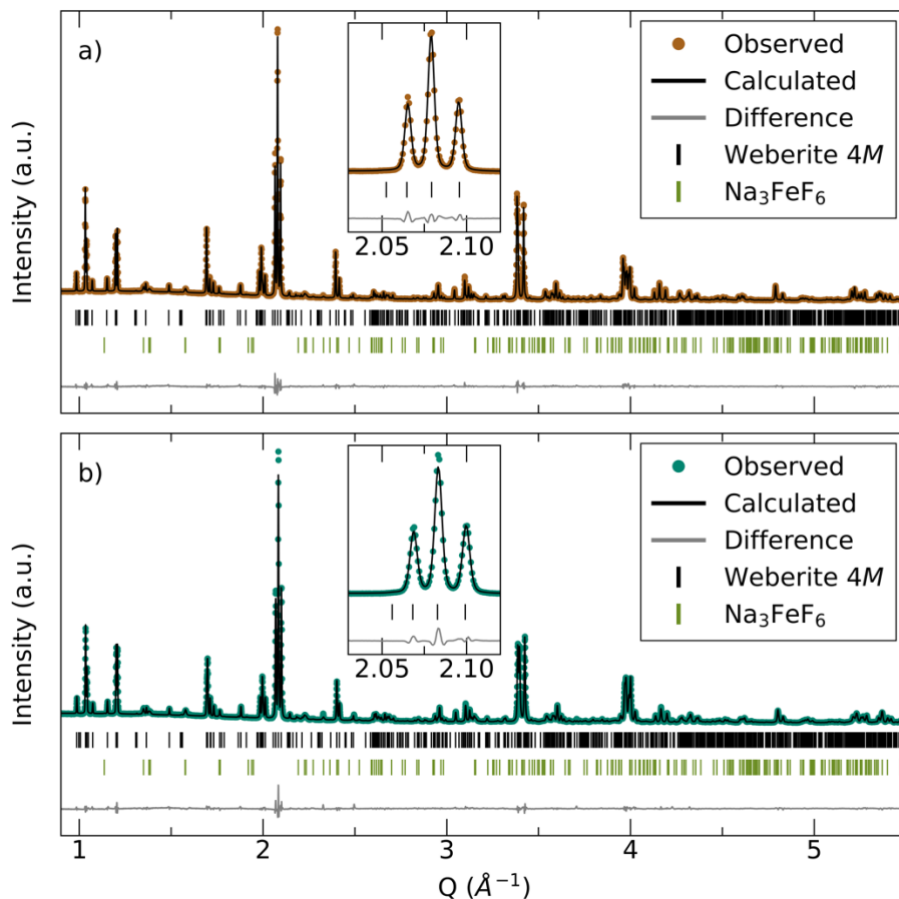

Figure 2. Synchrotron XRD characterization of as-prepared $Na_2Fe_2F_7$ (Mg0) and $Na_2Mg_{0.125}Fe_{1.875}F_7$ (Mg0.125) annealed at 650°C. Synchrotron XRD patterns of as-prepared (a) Mg0 and (b) Mg0.125 with corresponding Rietveld refinements (Mg0: $\chi^2 = 0.29$, $R_{WP} = 3.73$ and Mg0.125: $\chi^2 = 0.31$, $R_{WP} = 4.17$). The insets show the main weberite peaks in the Q range of 2.04–2.12 Å^{-1}.

Scanning electron microscopy (SEM) images of the as-synthesized powders (**Figure S12**) reveal that the Mg0.125 samples exhibit larger particle sizes at lower anneal temperatures than the Mg0 samples, thus Mg appears to improve crystallinity at intermediate anneal temperatures. Given that the samples annealed at 650°C showed the highest crystallinity, similar particle sizes, a low impurity content, and the best performance in our preliminary electrochemical tests, these were selected for the remainder of the study.

To prepare free-standing cathode films for electrochemical testing, carbon (C)-coated Mg0 and Mg0.125 powders were prepared by ball milling the as-prepared weberite powder for 12 h at 300 rpm with carbon black (Super P) and multiwalled carbon nanotubes (MWCNT) in a 70:15:5 (weberite : Super P : MWCNT) ratio by weight. SXRD patterns collected on the carbon (C)-coated Mg0 and Mg0.125 indicate that the weberite phase is largely retained upon carbon coating, with the weberite peaks still present and minimal change in the impurity content of the samples (**Figure S13** and **Table S10**). As the carbon coating process

leads to significant particle downsizing and broadening of the diffraction peaks, it introduces some uncertainty in the polymorphic content of the resulting carbon-coated samples. We therefore combined our SXRD analysis of the long-range crystal structure with ^{23}Na/^{19}F solid-state nuclear magnetic resonance (ss-NMR) and ^{57}Fe Mössbauer spectroscopy to monitor changes in the local structure around Na, F, and Fe species.

The ^{23}Na and ^{19}F ss-NMR spin echo spectra collected on the pristine and C-coated Mg0 and Mg0.125 samples are shown in **Figures 3** and **S14**, respectively. As Mg0 and Mg0.125 contain open-shell, redox-active Fe^{2+}/Fe^{3+} species, the ^{23}Na and ^{19}F ss-NMR spectra are dominated by strong electron-nuclear hyperfine (paramagnetic) interactions, leading to significant NMR line broadening and large-magnitude chemical shifts. Additionally, ^{23}Na is a quadrupolar nucleus ($I = 3/2$) and quadrupolar interactions contribute further line broadening and, at these low fields, to an additional, second-order quadrupole-induced shift of the observed resonances. The presence of multiple Na local environments in the samples results in significant signal overlap in the range from 600 to –400 ppm (**Figure 3**). The spectra can be fit using two resonances, which we tentatively attribute to Na in cubic and bihexagonal pyramidal sites in the weberite structure based on our previously-reported first principles NMR parameters obtained for $Na_2Fe_2F_7$.[51] Fits of the spectra collected before and after C-coating (**Figure S15** and **Table S11**) reveal only limited changes in the quadrupolar parameters (η_Q and C_Q) and line broadening, indicating that the local structure around Na is largely unchanged during the ball milling process. In fact, the observed spectral changes likely stem from increased local strain/disorder induced by the carbon coating process, and a greater distribution of Na local environments, with little change to the long-range weberite structure. Analysis of the ^{19}F ss-NMR and ^{57}Fe Mössbauer spectra (**Figures S16–18** and **Tables S12–14**) also indicate minor changes in the distribution of F and Fe local environments in the samples upon carbon coating, with a more detailed interpretation of these results provided in **Supplementary Notes 1** and **2**.
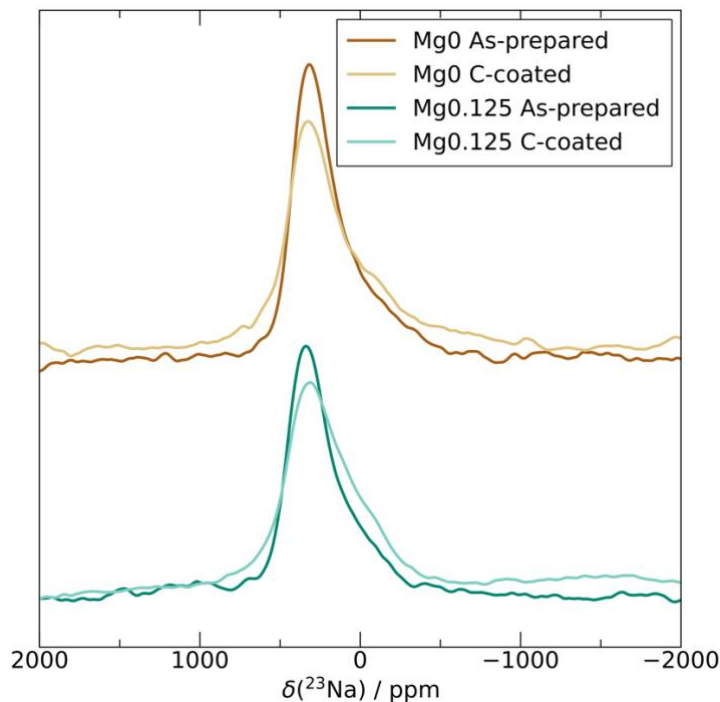
Figure 3. ^{23}Na ss-NMR characterization of as-prepared and carbon-coated Mg0 and Mg0.125 samples. ^{23}Na ss-NMR spin-echo spectra collected on as-prepared and carbon-coated Mg0 and Mg0.125 powder samples. Spectra were acquired at 2.35 T with a magic angle spinning (MAS) speed of 60 kHz using $\pi/6$ excitation pulses and a 20 ms recycle delay. Spectra were scaled by the number of scans taken and the sample mass.

Overall, using SXRD, we have confirmed the successful synthesis of single-polymorph ($4M$) $Na_2Fe_2F_7$ and $Na_2Mg_{0.125}Fe_{1.875}F_7$, with a minor (5–10 wt.%) Na_3FeF_6 impurity. The retention of the $4M$ structure upon electrode processing using ball milling is confirmed *via* ^{23}Na and ^{19}F ss-NMR and ^{57}Fe Mössbauer spectroscopy.

Impact of Mg substitution on the electrochemical behavior of the $Na_2Fe_2F_7$ cathode

Mg0 and Mg0.125 cathodes were tested in Na half cells to determine the impact of Mg substitution on the electrochemical behavior of $Na_2Fe_2F_7$. For this, free standing cathode films were prepared by combining the carbon-coated weberite and polytetrafluoroethylene (PTFE) in a 90:10 ratio by weight. Unless indicated otherwise, the cathodes were cycled galvanostatically at a rate of $C/20$ (full (dis)charge in 20 h, assuming two Na ions are transferred per formula unit and no parasitic side reactions), starting with a charge to 4.0 V *vs.* Na^+/Na.

To assess the impact of the cycling voltage window on the stability of the weberite structure, we compared electrochemical results obtained over the 2.8–4.0 V and 1.9–4.0 V ranges, respectively (**Figure 4**). The shapes of the first cycle voltage profiles and dQ/dV curves of Mg0 and Mg0.125 are similar, apart from the features near 2.4 V and 3.8 V on charge (2.1 V and 3.7 V on discharge) only present in the Mg0 data (**Figure S19**). The loss of these redox features at least partly accounts for the lower initial reversible capacity of Mg0.125 (72 and 45 mAh/g when discharging to 1.9 and 2.8 V, respectively) compared to Mg0 (92 and 58 mAh/g).
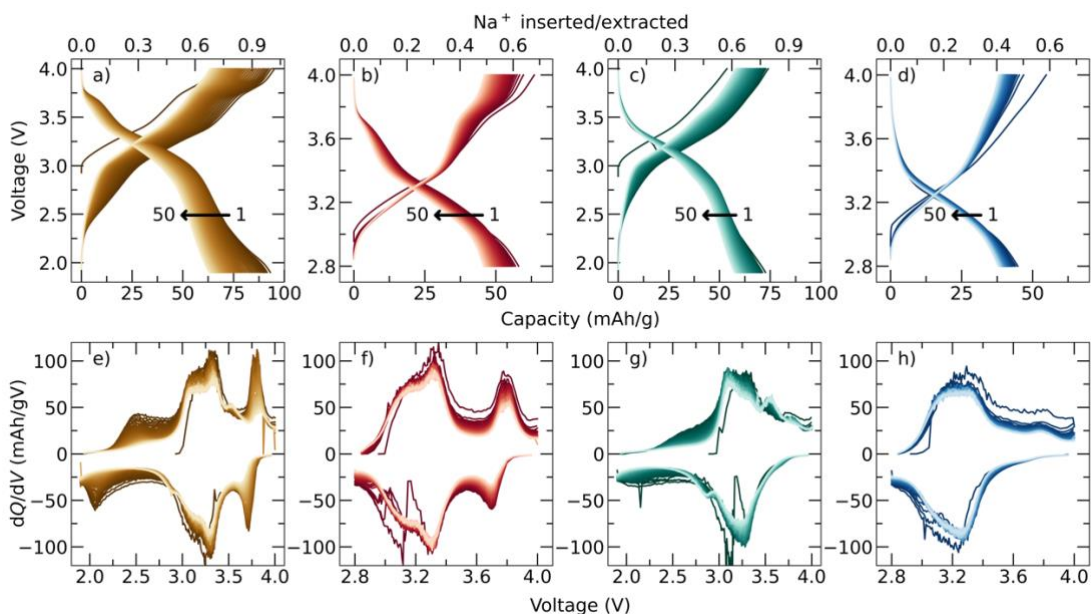

Figure 4. Electrochemical properties of Mg0 and Mg0.125. Galvanostatic charge-discharge curves, and resulting differential capacity plots recorded at $C/20$ over the first 50 cycles for Mg0 cycled between (a, b) 1.9 and 4.0 V, and between (e, f) 2.8 and 4.0 V, and for Mg0.125 cycled between (c, d) 1.9 and 4.0 V, and between (g, h) 2.8 and 4.0 V at 25°C. All cells exhibit coulombic efficiencies greater than 98% by cycle 10, enabled by the use of an ultra-dry (< 20 ppm of H_2O) electrolyte. In contrast, cells prepared with an electrolyte containing small amounts of water exhibit lower coulombic efficiencies of around 85%, as shown in **Figure S20**.

When limiting the cycling window to 2.8–4.0 V, the dQ/dV profiles of Mg0 and Mg0.125 do not evolve significantly upon extended cycling (detailed analysis in **Figures S21** and **S22**). In contrast, when Mg0 is

cycled between 1.9 and 4.0 V, we observe significant evolution of the dQ/dV curves (**Figure S23**), namely the fade of the weberite redox peaks at 3.80 and 3.35 V on charge, and at 3.75 and 3.25 V on discharge, and the growth of new redox peaks at 3.50 and 3.10 V on charge, and 2.90 V on discharge, first appearing between cycles 5 and 10. We assign these new dQ/dV peaks to redox processes in a new Na_yFeF_3 perovskite phase that emerges upon cycling, based on previous electrochemical studies of this material,[65,66] and based on our previous *ex situ* XRD and ss-NMR work indicating a gradual transformation of the weberite $Na_xFe_2F_7$ cathode to perovskite Na_yFeF_3 upon cycling. While the evolution of the Mg0.125 dQ/dV profile upon cycling between 1.9 and 4.0 V suggests some amount of transformation to a perovskite phase analogous to Na_yFeF_3, first apparent between cycles 5 and 10, and stabilizing by cycle 15 (**Figure S24**), the redox peaks of the weberite phase are much better retained than in the case of Mg0. Nevertheless, the low voltage redox features initially observed in the dQ/dV curves of the two cathodes steadily fade upon extended cycling over the large voltage window, indicating a common degradation mechanism preventing the (de)intercalation of some Na sites in the weberite structure.

The absolute discharge capacity and capacity retention (in %) of Mg0 and Mg0.125 are plotted for the first 50 cycles in **Figures 5a** and **5b**, respectively. When using a narrow voltage window (2.8–4.0 V), the two cathodes exhibit improved reversibility, with 79% and 85% discharge capacity retention after 50 cycles. When Mg0 is cycled between 1.9 and 4.0 V, larger initial discharge capacities are observed, as mentioned earlier, but this is accompanied by significant capacity fade, with only 69% capacity retention over 50 cycles. While Mg0.125 exhibits lower initial discharge capacities than Mg0, the cycling stability relative to Mg0 is significantly improved, with 82% retention of the initial discharge capacity over 50 cycles. Those results are consistent with the gradual transformation of Mg0 to Na_yFeF_3 over the 50 cycles, and the better preservation of the weberite structure and of its redox properties for Mg0.125.
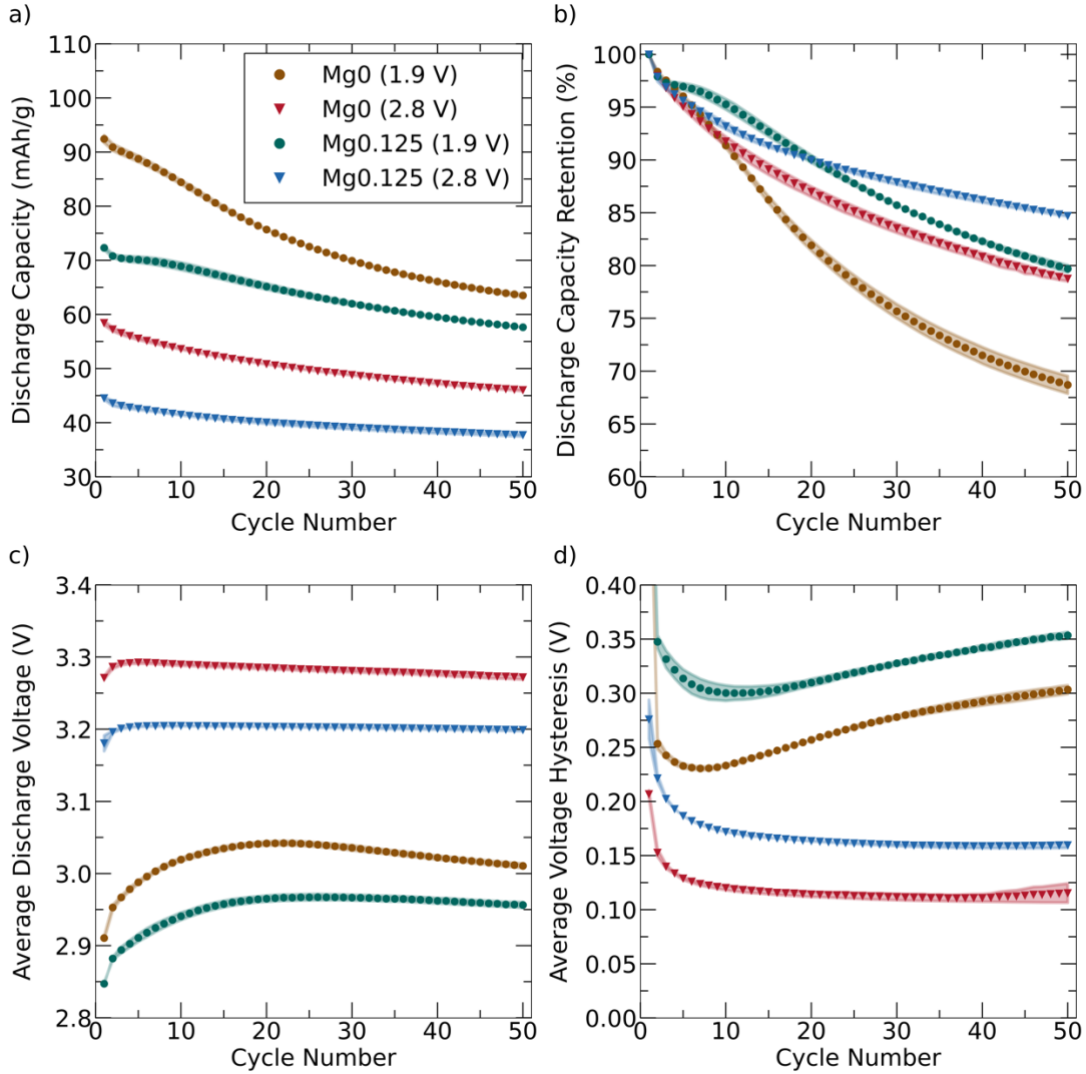
Figure 5. Evolution of various electrochemical performance metrics of Mg0 and Mg0.125 over the first 50 cycles. (a) Absolute discharge capacity, (b) capacity retention (in %), (c) average voltage, (d) and voltage hysteresis observed during the first 50 cycles at a rate of *C*/20 and at 25°C for Mg0 and Mg0.125 and using the 2.8–4.0 V and 1.9–4.0 V voltage windows. The shaded regions delineate the range of values obtained at each cycle for duplicate cells, with the symbols representing the average value.

The average discharge voltage and voltage hysteresis over the first 50 cycles are plotted as a function of cycle number in **Figures 5c** and **5d** for Mg0 and Mg0.125 cycled over both voltage windows. Increasing the lower voltage cutoff from 1.9 V to 2.8 V reduces the 10th cycle average discharge voltage from 3.29 V to 3.20 V for the narrower voltage window (2.8–4.0 V), and from 3.02 to 2.94 V for the wider voltage window (1.9–4.0 V) for Mg0 and Mg0.125 respectively. Importantly, the average discharge voltage for Mg0.125 is generally lower than that of Mg0, which can be accounted for by the loss of the high voltage plateau in the Mg0.125 voltage profile. Additionally, Mg0.125 exhibits a higher voltage hysteresis than Mg0, of 0.30 V compared to 0.24 V (0.17 V compared to 0.12 V) on the 10th cycle when using a large (small) voltage window. The reduced capacity at high voltages, and larger voltage hysteresis observed for Mg0.125 suggest that Mg substitution hinders Na extraction at high potentials.

To investigate the potential kinetic limitations induced upon Mg incorporation, we cycled Mg0 and Mg0.125 at elevated temperature (50°C) and over the wider (1.9–4.0 V) and narrower (2.8–4.0 V) voltage windows (**Figures S26–S23**). Overall, the initial capacities are increased at 50°C, reaching 122 and 96 mAh/g for the larger voltage window, and 70 and 56 mAh/g for the narrower voltage window, for Mg0 and Mg0.125, respectively. However, worse capacity fade and a more rapid evolution of the dQ/dV profiles is observed over time, which is presumably a manifestation of the underlying transformation to Na_yFeF_3 and is consistent with battery fade mechanisms accelerating at elevated temperature. Mg0.125 still exhibits a lower capacity than Mg0, but enhanced capacity retention, particularly when using the wider voltage window. Mg0.125 exhibits a 21% lower discharge capacity relative to Mg0 when cycling over the 2.8–4.0 V range, and a 20% lower discharge capacity when cycling over the 1.9–4.0 V range at 50°C. These differences between the two cathodes are only slightly lower than at 25°C, where a 22% reduction in discharge capacity is observed for Mg0.125. While the capacity limitations in Mg0.125 appear to be kinetic in nature, they are not overcome at 50°C. In contrast, the voltage hysteresis of the Mg-substituted cathode is reduced at 50°C, whereas that of the all-Fe compound remains approximately the same. As a result, the difference in voltage hysteresis between the two cathodes is much reduced at elevated temperatures, suggesting that these differences are dominated by kinetics (**Figure S26**). This is accompanied by a narrowing of the difference between the average discharge potentials of Mg0.125 and Mg0.

To gain further insights into the kinetics of the Na (de)intercalation processes, galvanostatic intermittent titration technique (GITT) tests were performed on the cathodes at 25°C and 50°C over the 1.9–4.0 V voltage range (**Figure 6**). Large overpotentials are observed at the voltage extrema (particularly pronounced at low voltages), which decrease at elevated temperature, as expected. The overpotentials observed for Mg0.125 are larger than for Mg0 across the entire voltage range at room temperature, and are particularly large at high voltages (0.28 V for Mg0.125, and 0.18 V for Mg0 at 3.9 V). Furthermore, the overpotential of the Mg0.125 cathode cycled at 50°C becomes similar to that of the Mg0 cathode, again suggesting kinetic limitations to Na extraction/reinsertion in the Mg-substituted cathode that are partially overcome at elevated temperatures.
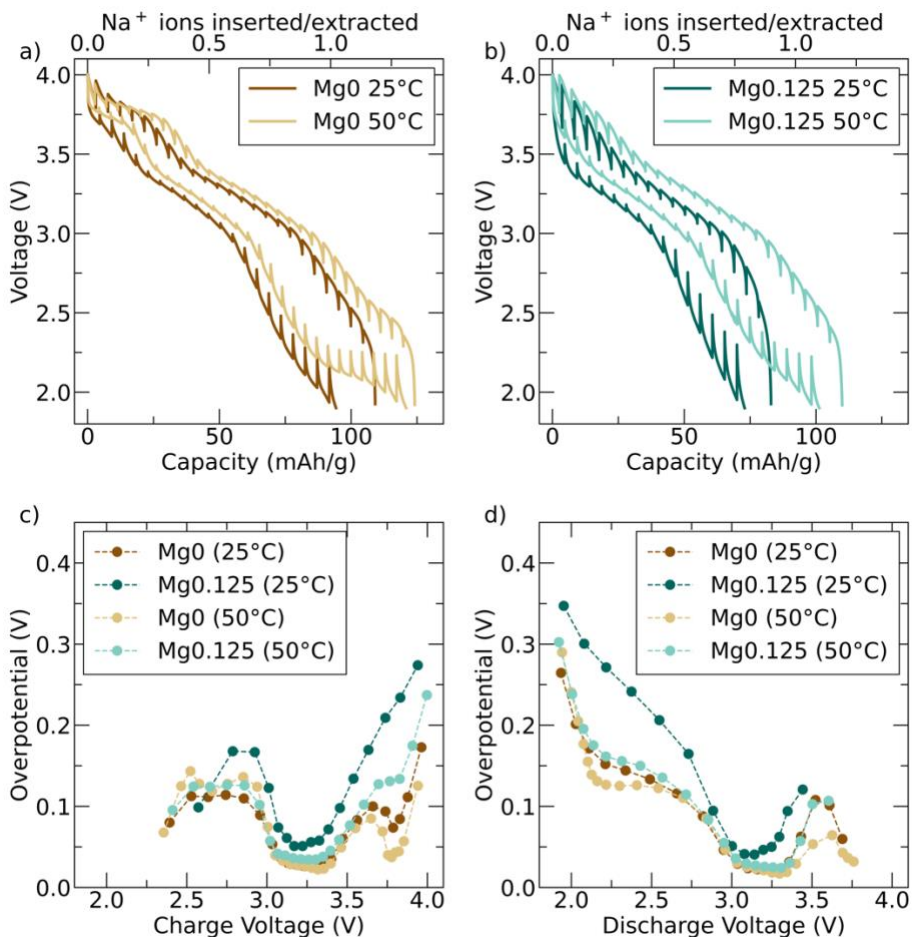
Figure 6. GITT data obtained during the second charge-discharge cycle where 30 min *C*/20 current pulses were applied before a 2 h rest period between 1.9 and 4.0 V at 25°C and 50°C, for (a) Mg0 and (b) Mg0.125. The measured overpotentials are plotted a function of (c) charge and (d) discharge voltages for the two cathodes and at both temperatures, where these voltages are the voltages achieved before the relaxation step. Active material loadings were 2.9 mg/cm² for the 50°C cells and 2.6 mg/cm² for the 25°C cells for both compositions.

The rate performance of Mg0 and Mg0.125 was also tested over the narrower 2.8–4.0 V voltage range at 25°C to eliminate the large overpotentials at low voltages revealed by GITT. For Mg0, 78% of the initial capacity at *C*/20 is retained at *C*/5, which quickly falls off as the rate is increased to 1*C* and beyond. Mg0.125 displays worse rate performance, with only 62% capacity retention at *C*/5, which also quickly falls off at higher rates (**Figure 7**). This indicates that Na (de)intercalation is kinetically limited in both systems, but more severely limited in Mg0.125.
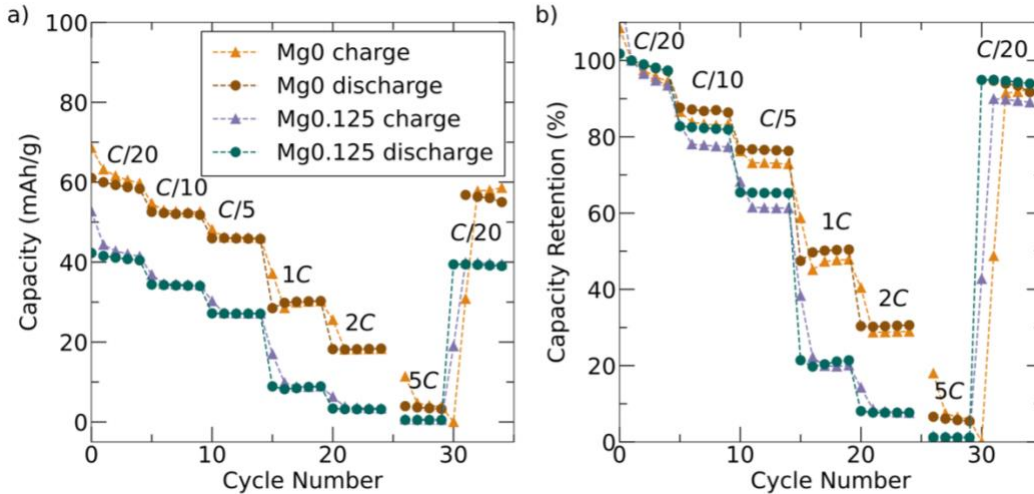
Figure 7. Charge and discharge capacities and capacity retention obtained over 5 galvanostatic cycles (for a total of 35 cycles) at cycling rates of *C*/20, *C*/10, *C*/5, 1*C*, 2*C*, 5*C*, and C/20 in the voltage range 2.8 to 4.0 V at 25°C.

Thus, while Mg0.125 demonstrates improved cycling stability relative to Mg0, its reduced capacity is due to kinetically limited Na (de)intercalation.

Discussion

The results presented herein demonstrate the synthesis of a single 4*M* polymorph (space group *C*2/c) of the $Na_2Fe_2F_7$ (Mg0) and $Na_2Mg_{0.125}Fe_{1.875}F_7$ (Mg0.125) weberites, and provide a detailed account of these materials' structural and electrochemical properties. Notably, the preparation of single-polymorph weberites contrasts with our previous work, where the coexistence of 2*O*, 3*T*, and 4*M* polymorphs was observed in Mg0 samples.[51] We hypothesize that this discrepancy is due to the faster quenching step employed herein, enabling more effective stabilization of the 4*M* polymorph. Additionally, the stabilization of the 4*M* polymorph goes counter to our DFT predictions suggesting a lower energy 3*T* polymorph for both Mg0 and Mg0.125, but this may be explained by the very small difference in decomposition energy (< 5 meV/at) between these polymorphs. Since our 0 K DFT calculations only consider the enthalpy of these systems, it is possible that the lower symmetry *4M* polymorph is entropically or kinetically stabilized at the relevant annealing temperatures.

Electrochemical testing using a 4.0 V upper cutoff voltage reveals that increasing the lower voltage cutoff from 1.9 to 2.8 V leads to a drastic increase in capacity retention over the first 50 cycles, from 69% to 79% for the Mg0 cathode, while a significant increase in capacity retention from 69% to 82% is observed over the larger voltage window upon Mg substitution. These improvements in performance are attributed to better preservation of the metastable weberite structure (i.e., no transformation to the more stable perovskite structure, consistent with our previous work[51]), and suggests that high levels of Na (de)intercalation ($x > 2$) are detrimental to the stability of the all-Fe weberite cathode, while Mg substitution has a beneficial effect. The rapid decrease in capacity of the Mg0 cathode over the large voltage window may be explained by the lower redox capacity of the perovskite Na_yFeF_3 phase relative to the initial weberite phase,[66] and/or HF generation during this process (e.g., $Na_xFe_2F_7 + (2y - x)$ Na $\xrightarrow{\text{electrolyte}}$ 2 Na_yFeF_3 + HF), degrading the electrode surface and promoting further phase transformation.

We note that the most significant evolution of the Mg0 dQ/dV profile when cycling this cathode between 1.9 and 4.0 V is the fading of the weberite redox features at 2.4 V and 3.8 V (which are never observed upon cycling the Mg0.125 cathode). When both Mg0 and Mg0.125 are cycled in the voltage range 1.9–3.6 V (results not shown here), excluding the high-voltage plateau at 3.8 V for Mg0, we find that the improved cycling stability of Mg0.125 is maintained due to the absence of the low-voltage plateau at 2.4 V, which quickly fades in Mg0. This highlights the significance of both high- and low-voltage features in explaining the enhanced cycling stability with Mg substitution. While such changes could be due to structural degradation processes other than transformation of the weberite phase, the 3.8 V feature is retained when Mg0 is cycled between 2.8 and 4.0 V and there is no significant phase transformation, suggesting a relationship between the two.

Overall, Mg substitution for Fe in $Na_2Fe_2F_7$ stabilizes the weberite structure, but it also results in a reduced reversible capacity beyond what is expected from substituting a small amount of redox-active Fe^{2+} by Mg^{2+}. Given that only the Fe^{2+}/Fe^{3+} redox couple has been found to be electrochemically active in the all-Fe weberite,[50,51] one would anticipate 0.875 Na per formula unit to be extractable from Mg0.125, corresponding to a compositional change from $Na_2Mg^{2+}_{0.125}Fe^{2+}_{0.875}Fe^{3+}F_7$ to $Na_{1.125}Mg^{2+}_{0.125}Fe^{3+}_{1.875}F_7$, as opposed to 1 Na per formula unit for Mg0 or $Na_2Fe_2F_7$. Hence, a 12.5% reduction in capacity is expected for the Mg-substituted cathode, but instead Mg0.125 cycles approximately 22% less Na than Mg0. The additional capacity limitations observed for Mg0.125 result from sluggish Na(de)intercalation from the structure, particularly at high voltage, and are likely due to more sluggish Na diffusion in the structure, as we do not expect the electronic conductivities of these highly electronically insulating fluorides to be significantly different. Inspection of the dQ/dV profile of Mg0.125 cycled in the larger voltage window at 50°C reveals small peaks associated with Na extraction at the voltage extrema, which are absent for this cathode at room temperature. Hence, we hypothesize that Na diffusion is kinetically limited due to structural or electrostatic changes[67] to the Na diffusion pathways upon Mg substitution, rather than Mg diffusion resulting in obstruction within the Na diffusion pathways in this material.

Conclusions

In this work, we explored the effects of isovalent Fe^{2+} substitution by electrochemically inactive Mg^{2+} on the structural and electrochemical properties of the intercalation-type $Na_2Fe_2F_7$ weberite cathode material. In particular, our choice of substituent was informed by density functional theory calculations, suggesting improved stability of $Na_2Mg_xFe_{2-x}F_7$ compounds as the Mg content is increased. We demonstrated the synthesis of a single $4M$ polymorph (space group $C2/c$) of the $Na_2Fe_2F_7$ (Mg0) and $Na_2Mg_{0.125}Fe_{1.875}F_7$ (Mg0.125) weberites using synchrotron X-ray diffraction. Local structure probes, namely [23]Na and ^{19}F solid-state nuclear magnetic resonance and [57]Fe Mössbauer spectroscopy, indicate good retention of the weberite structure upon mechanochemical milling in preparation for electrochemical testing, despite its metastability. We find that Mg0.125 displays far more reversible cycling than Mg0 over a 1.9-4.0 V window (82 % and 69% capacity retention over 50 cycles for Mg0.125 and Mg0, respectively), which is attributed to a reduced transformation from the metastable weberite phase to a more stable perovskite phase. This phase transformation is eliminated upon using a 2.8 V lower voltage cutoff for both cathode compositions. Despite the improved cycling stability of Mg0.125, this material also displays a significant (22%) reduction in capacity relative to Mg0, beyond what is expected from simple replacement of redox-active Fe^{2+} species by redox-inactive Mg^{2+}. Using high-temperature galvanostatic cycling, GITT, and variable rate cycling, we were able to demonstrate that the low capacity of Mg0.125 is related to limitations in the rate and extent of Na (de)intercalation, particularly at high voltages. Overall, this work shows that compositional substitution is a viable path towards developing more stable weberite cathodes that enable more reversible

electrochemical cycling. However, due to the kinetic limitations caused by partial Mg incorporation, other compositional substitutions of Fe in $Na_2Fe_2F_7$ must be pursued to both improve the intrinsic stability of the weberite structure upon cycling and retain the capacity and energy density of the all-Fe system. Other compositions, including those moving beyond Fe redox, may hold the key for a high-capacity and energy-dense, yet stable weberite cathode.

Methods

Material Synthesis

$Na_2Fe_2F_7$ (Mg0) and $Na_2Mg_{0.125}Fe_{1.875}F_7$ (Mg0.125) were prepared via a mechanochemical-assisted solid state synthesis. All precursors and prepared materials were handled in an argon glovebox, sealed in argon, or placed under argon gas flow throughout this synthesis as fluorides react readily with water to form hydrofluoric acid. A stoichiometric mixture totaling 1 g of vacuum-dried binary fluoride precursors—NaF (Sigma-Aldrich, 99.99%), FeF_2 (Sigma-Aldrich, 98%), MgF_2 (Sigma-Aldrich, 99.9%), FeF_3 (Strem Chemicals, 99%)—were hand-mixed and sealed into a 50 mL ZrO_2 jar in an argon glovebox with five 10 mm and ten 5 mm ZrO2 balls and subsequently ball-milled for 24 h at 400 rpm. After 6–12 h, the ball milling process was halted and the ball-mill jar was unsealed to scrape the precursor mixture from the lid and rim of the jars back into the jar, ensuring complete reaction of the precursors. The ball-milled powders were then pelletized and annealed at 425°C, 500°C, 575°C, or 650°C for 30 minutes under argon gas flow. After annealing, the pellets were quickly cooled by moving the alumina tube, which held the annealed pellets in an alumina crucible, horizontally in the tube furnace. This action removed the pellets from the heating element, and the outside of the alumina tube was cooled with compressed air until it was cool to the touch, all while keeping the pellets under argon gas flow to prevent air and water exposure. The pellets were then hand ground, and the resulting powder was further characterized in the as-prepared state and processed into composite electrodes for electrochemical testing.

Material Characterization.

X-ray Diffraction

Samples were packed and sealed in glass capillaries to minimize air exposure during measurement. High resolution synchrotron powder diffraction patterns for the pristine materials were collected on Experimental Station 2-1 at the Stanford Synchrotron Radiation Lightsource, SLAC National Accelerator Laboratory, using an average wavelength of 0.7294335 Å between 2θ of 1.5 and 105° at room temperature. For the carbon-coated materials, high resolution powder diffraction patterns were collected on Beamline I-11 at Diamond Light Source, using an average wavelength of 0.824104 Å between 2θ of 6 and 92° at room temperature. Laboratory X-ray diffraction data was acquired on a Panalytical Empyrean Powder Diffractometer using a Copper K-α source (wavelength of 1.5406 Å) between 2θ of 10 and 90°, summing 5 scans. Samples were kept air-free during laboratory X-ray diffraction using a sealed Kapton®-tape-based container. Diffraction patterns were analyzed via initial Pawley fits to determine peak shape fitting parameters, followed by Rietveld refinements using the TOPAS software (v7).[68] Our refinement procedure can be summarized as follows: First, we refined the X-ray wavelength and the zero error using a Si reference. Next, Pawley fits were conducted to establish initial peak shape fitting parameters. During the Rietveld analysis, we refined lattice parameters, atomic positions, and site occupancies (with Mg and Fe site occupancies in the shared sites constrained to sum to one), along with thermal parameters (which were

constrained to be the same for each element across all phases). Lastly, peak shape fitting parameters, including Lorentzian and Gaussian strain and particle size contributions, were allowed to vary. Crystal structures were depicted using VESTA 3.[69]

Scanning Electron Microscopy

SEM images were acquired using a Thermo Fisher Apreo C LoVac SEM instrument with an accelerating voltage of 5 keV and a current of 0.4 nA.

[23]Na Solid-State Nuclear Magnetic Resonance

^{23}Na ss-NMR data were collected on Mg0 and Mg0.125 as-synthesized and carbon-coated samples using a Bruker Avance 100 MHz (2.35 T) wide-bore NMR spectrometer with Larmor frequencies of 26.48 MHz at room temperature. The data were obtained at room temperature and under a 60 kHz magic-angle spinning (MAS) speed (corresponding to approximately 318 K sample temperature) using a home-built 1.3 mm double-resonance HX probe. ^{23}Na NMR data were referenced against 1M aqueous solutions of sodium chloride [NaCl, δ([23]Na) = 0ppm], and these samples were also used for pulse calibration. [23]Na spin-echo spectra were acquired on all samples using $\pi/2-\pi-\pi/2$ and $\pi/6-\pi/3-\pi/6$ rotor-synchronized spin echo pulse sequences to selectively excite less quadrupolar environments and equally excite all environments, respectively. The radiofrequency (RF) pulse lengths were 0.23 µs for $\pi/6$, 0.46 µs for $\pi/3$, 0.7 µs for $\pi/2$, and 1.4 µs for π at a power of 38 W. A recycle delay of 20 ms was used to ensure that the full [23]Na signal was fully relaxed between pulses. Spectra were fit using the int2Quad model in DMFit.[70]

[19]F Na Solid-State Nuclear Magnetic Resonance

^{19}F ss-NMR data were collected on the as-synthesized and carbon-coated Mg0 and Mg0.125 samples using a Bruker Avance 100 MHz (2.35 T) wide-bore NMR spectrometer with Larmor frequencies of 94.08 MHz at room temperature. The data were obtained at 60 kHz MAS using a 1.3 mm double-resonance HX probe. ^{19}F ss-NMR data were referenced against 1M aqueous solutions of sodium fluoride [NaF, δ(^{19}F) = −118 ppm], which also used for pulse calibration. The RF pulse lengths used in the rotor-synchronized spin echo pulse sequence were 0.3 µs for $\pi/2$ and 0.6 µs for π (power of 5 W). A recycle delay of 20 ms was used for each sample to ensure that the bulk (paramagnetic) ^{19}F signal was fully relaxed between pulses. Spectra were fit using the CSA MAS model in DMFit.[70]

To quantify the signals, between 6 and 8 wt.% of MgF_2 was added to as-prepared Mg0 and Mg0.125 samples, hand ground, and added to 1.3 mm rotors. For these ^{19}F ss-NMR spectra, The RF pulse lengths used in the rotor-synchronized spin echo pulse sequence were 1.6 µs for $\pi/2$ and 3.2 µs for π (power level of 19 W). A recycle delay of 38 s was used for each sample to ensure that the full ^{19}F signal of diamagnetic MgF_2 was completely relaxed between pulses. Spectra were fit using the CSA MAS model in DMFit.[70] Longitudinal (T_1) and transverse (T_2) relaxation values were measured for each signal and calculated from inversion recovery and spin-echo experiments (where the echo delay is systematically increased) using Topspin (v 4.3.0). The signals were quantified via integration of each signal, which was then T_2 corrected.

[57]Fe Mössbauer Spectroscopy

Room-temperature [57]Fe Mössbauer spectroscopy was performed using a SEECo Model W304 resonant gamma-ray spectrometer (activity ~ 16 mCi due to the age of the source, [57]Co/Rh source) equipped with a Janis Research Model SVT-400 cryostat system. The source linewidth was < 0.26 mm s^{-1} for the innermost lines of a 25 µm α-Fe foil standard. Isomer shifts were referenced to α-Fe foil at room temperature. All samples consisted of 40-52 mg of the material loaded into a plastic holder in an Ar glovebox, capped, and

then measured under a positive flow of nitrogen at room temperature. The data were fit using the MossA software.[71]

Electrochemical Characterization

The as-synthesized Mg0 and Mg0.125 samples were mechanochemically carbon coated prior to electrochemical testing to ensure electronically conductive composite electrodes. Pristine Mg0 and Mg0.125 (annealed at 650°C) were combined with carbon black (Super P, MTI Corporation) and multi-walled carbon nanotubes (MWCNT, Sigma-Aldrich, 98%) in a 70:15:5 (weberite : Super P : MWCNT) ratio, added into a 50 mL ZrO_2 ball mill jar sealed under Ar with three 10 mm and three 5 mm ZrO_2 balls, and ball-milled at 300 rpm for 12 h. The resulting carbon-coated materials were hand-ground with 10 wt. % polytetrafluoroethylene (Sigma-Aldrich) and rolled into free standing film electrodes. For standard electrochemical testing, 10 mm diameter electrodes were punched with loading densities ranging from 1.8 to 2.6 mg/cm^2 (calculated based on the mass of the active material in the electrode), and assembled into CR2032-type coin cells with a Na metal (Sigma-Aldrich) anode, glass fiber separator (Whatman GF/D), and 160 μL of an in-house prepared electrolyte consisting of 1 M $NaPF_6$ (Strem Chemicals, 99%) in propylene carbonate (Sigma-Aldrich, 99.7%) with 2 vol % fluoroethylene carbonate (Sigma-Aldrich, ≥ 99%) with < 20 ppm of H_2O as determined by Karl Fisher analysis.

For galvanostatic measurements, current corresponding to a C/20 rate (full (dis)charge in 20 h calculated from the theoretical capacity of each composition assuming two Na-ions are transferred per formula unit, and assuming no parasitic side reactions take place) was applied and the cell was cycled in the voltage range 1.9–4.0 V or 2.8–4.0 V. For GITT measurements, the cell was cycled galvanostatically at C/20 for a full cycle and GITT data obtained over the second cycle, where a 30 min C/20 current pulse was applied, followed by a 2h rest period. During variable rate cycling, galvanostatic charge-discharge curves were obtained for 5 cycles at each rate—C/20, C/10, C/5, 1C, 2C, and C/20 again—for a total of 35 cycles.

Computational Characterization.

DFT calculations were performed using the Vienna ab initio Simulation Package (VASP).[72–75] VASP calculations used projector augmented wave pseudopotentials (Na pv, Fe, Mg, and F),[76,77] built for use with the strongly constrained and appropriately normed (SCAN)-based functionals,[78] a plane-wave energy cutoff of 700 eV, and the restored regularized strongly constrained and appropriately normed (r^{2}SCAN)[63] functional with the Hubbard U correction. The Hubbard U correction[79] has recently been shown to be necessary to correct for unphysical electron-self interaction effects, even in the meta-Generalized Gradient Approximation (meta-GGA) SCAN and r^{2}SCAN functionals.[80,81] A U value of 5.4 eV was used for Fe based on a recent preprint that has optimized this value specifically for transition metal fluorides for the r^{2}SCAN functional.[64] We also performed the same calculations using a U value of 3.1 eV,[80] which has been optimized for transition metal oxides, as has generally been previously applied to transition metal fluorides in lieu of appropriately optimized values for fluorides (see supplementary information). Calculations using the Perdew−Burke−Ernzerhof generalized-gradient approximation (GGA)[82] functional with the Hubbard U correction ($U_{Fe} = 4.0$ eV, as optimized for oxides)[83,84] utilized a plane wave cutoff energy of 520 eV, and the same convergence criteria and reciprocal space sampling as listed below.

Calculations pertaining to the $Na_2Fe_2F_7$ (Mg0), $Na_2Mg_xFe_{2-x}F_7$ (*x = 0.25, 0.5, 0.75*), and $Na_2Fe_{2-x}Al_xF_7$ (*x = 0.25, 0.5, 0.75*) 2O and 3T structures were performed on $1 \times 1 \times 1$ ferromagnetically-ordered conventional

unit cells (44 and 66 atoms respectively). Calculations pertaining to the $Na_2Fe_2F_7$ (Mg0), $Na_2Mg_xFe_{2-x}F_7$ ($x = 0.125, 0.25, 0.5, 0.75$), and $Na_2Fe_{2-x}Al_xF_7$ ($x=0.25, 0.5, 0.75$) 4M structures were performed on $1 \times 1 \times 1$ ferromagnetically-ordered primitive unit cells (88 atoms). To achieve the appropriate stoichiometries for $Na_2Mg_{0.125}Fe_{1.875}F_7$ (Mg0.125), a $1 \times 1 \times 2$ supercell of the parent $Na_2Fe_2F_7$ 2O structure was utilized (again ferromagnetically ordered, 88 atoms). As the required supercell to achieve the $x = 0.125$ stoichiometry for the 3T structure was prohibitively large (264 atoms), calculations for the $x = 0.166$ stoichiometry were performed using a $1 \times 1 \times 1$ ferromagnetically-ordered conventional unit cell of the parent structure and calculations for the $x = 0.0833$ stoichiometry utilized a $1 \times 1 \times 2$ ferromagnetically-ordered conventional unit cell (132 atoms). These energies were averaged to achieve an estimate for the energy of the 3T Mg0.125 structure. For structures containing Mg^{2+} substitution on the Fe^{2+} sites or Al^{3+} substitution on the Fe^{3+} sites, symmetrically unique Mg^{2+}–Fe^{2+} and Al^{3+}–Fe^{3+} orderings were enumerated and ranked according to their Ewald sum energy as implemented in Pymatgen,[85] with the five lowest energy structures considered, except for the Mg0.125 ($x = 0.125$) calculations, which considered the two lowest energy structures, and the fifth lowest energy structure due to computational cost associated with the the large unit cell sizes resulting from this stoichiometry. The structures were fully relaxed (atomic positions and cell parameters) and final energies were obtained by a final static calculation. The convergence criteria for the total electronic energy and interatomic forces were 10^{-5} eV and 0.01 eV/Å respectively, with Gaussian smearing with a width of 0.05 eV and a k-point spacing of 25 Å^{-1} centered at Γ.

Decomposition energies were calculated by first calculating the energies of all relevant binary or ternary fluoride phases (phases considered are listed in **Table S2**) in a similar approach to above, using the r^{2}SCAN functional and considering both Hubbard U values of 3.1 and 5.4 eV. Decomposition pathways were enumerated using the Reaction Network python package,[86] and decomposition energies were subsequently calculated using the DFT-obtained energy values. The most spontaneous (most favorable) pathway (as tabulated in **Table S1**) was taken to be the decomposition pathway and its energy was taken to be the decomposition energy for each composition.

Conflicts of Interest

There are no conflicts of interest to declare.

Supporting Information

Crystal structure diagrams; DFT phase stability comparisons; diffraction patterns and Rietveld refinement results; scanning electron microscopy images; NMR spectra, fits, and quantification; Mössbauer spectra and fits; and additional electrochemical data.

Acknowledgements

References

(1) Goodenough, J. B.; Park, K.-S. The Li-Ion Rechargeable Battery: A Perspective. *J. Am. Chem. Soc.* **2013**, *135* (4), 1167–1176. https://doi.org/10.1021/ja3091438.

(2) Manthiram, A. A Reflection on Lithium-Ion Battery Cathode Chemistry. *Nat Commun* **2020**, *11* (1), 1550. https://doi.org/10.1038/s41467-020-15355-0.

(3) Kim, T.; Song, W.; Son, D.-Y.; Ono, L. K.; Qi, Y. Lithium-Ion Batteries: Outlook on Present, Future, and Hybridized Technologies. *J. Mater. Chem. A* **2019**, *7* (7), 2942–2964. https://doi.org/10.1039/C8TA10513H.

(4) S. Rangarajan, S.; Sunddararaj, S. P.; Sudhakar, A. V. V.; Shiva, C. K.; Subramaniam, U.; Collins, E. R.; Senjyu, T. Lithium-Ion Batteries—The Crux of Electric Vehicles with Opportunities and Challenges. *Clean Technologies* **2022**, *4* (4), 908–930. https://doi.org/10.3390/cleantechnol4040056.

(5) Zhu, Z.; Jiang, T.; Ali, M.; Meng, Y.; Jin, Y.; Cui, Y.; Chen, W. Rechargeable Batteries for Grid Scale Energy Storage. *Chem. Rev.* **2022**, *122* (22), 16610–16751. https://doi.org/10.1021/acs.chemrev.2c00289.

(6) Olivetti, E. A.; Ceder, G.; Gaustad, G. G.; Fu, X. Lithium-Ion Battery Supply Chain Considerations: Analysis of Potential Bottlenecks in Critical Metals. *Joule* **2017**, *1* (2), 229–243. https://doi.org/10.1016/j.joule.2017.08.019.

(7) Vaalma, C.; Buchholz, D.; Weil, M.; Passerini, S. A Cost and Resource Analysis of Sodium-Ion Batteries. *Nat Rev Mater* **2018**, *3* (4), 1–11. https://doi.org/10.1038/natrevmats.2018.13.

(8) S. Sharma, S.; Manthiram, A. Towards More Environmentally and Socially Responsible Batteries. *Energy & Environmental Science* **2020**, *13* (11), 4087–4097. https://doi.org/10.1039/D0EE02511A.

(9) Vera, M. L.; Torres, W. R.; Galli, C. I.; Chagnes, A.; Flexer, V. Environmental Impact of Direct Lithium Extraction from Brines. *Nat Rev Earth Environ* **2023**, *4* (3), 149–165. https://doi.org/10.1038/s43017-022-00387-5.

(10) U.S. Geological Survey. Mineral commodity summaries 2024. 2024. https://doi.org/10.3133/mcs2024

(11) Rudola, A.; R. Rennie, A. J.; Heap, R.; Shayan Meysami, S.; Lowbridge, A.; Mazzali, F.; Sayers, R.; J. Wright, C.; Barker, J. Commercialisation of High Energy Density Sodium-Ion Batteries: Faradion's Journey and Outlook. *Journal of Materials Chemistry A* **2021**, *9* (13), 8279–8302. https://doi.org/10.1039/D1TA00376C.

(12) Contemporary Amperex Technology Co., Ltd. *CATL Unveils Its Latest Breakthrough Technology by Releasing Its First Generation of Sodium-ion Batteries.* Contemporary Amperex Technology Co., Ltd., July 21, 2021. https://www.catl.com/en/news/665.html (accessed 2024-07-12).

(13) Hu, Y.-S.; Li, Y. Unlocking Sustainable Na-Ion Batteries into Industry. *ACS Energy Lett.* **2021**, *6* (11), 4115–4117. https://doi.org/10.1021/acsenergylett.1c02292.

(14) Xue, Y. China's first sodium-ion battery energy storage station could cut reliance on lithium. *South China Morning Post (Hong Kong),* May 14, 2024. https://www.scmp.com/business/article/3262522/chinas-first-sodium-ion-battery-energy-storage-station-could-cut-reliance-lithium (accessed 2024-07-12)

(15) Rudola, A.; Sayers, R.; Wright, C. J.; Barker, J. Opportunities for Moderate-Range Electric Vehicles Using Sustainable Sodium-Ion Batteries. *Nat Energy* **2023**, *8* (3), 215–218. https://doi.org/10.1038/s41560-023-01215-w.

(16) Ren, D. Chinese EV maker JAC unveils world's first car powered by cheaper sodium-ion battery. *South China Morning Post (Hong Kong),* February 24, 2023. https://www.scmp.com/business/china-business/article/3211430/chinese-ev-maker-jac-unveils-worlds-first-car-powered-cheaper-sodium-ion-battery (accessed 2024-07-12)

(17) Wang, P.; You, Y.; Yin, Y.; Guo, Y. Layered Oxide Cathodes for Sodium-Ion Batteries: Phase Transition, Air Stability, and Performance. *Advanced Energy Materials* **2018**, *8* (8), 1701912. https://doi.org/10.1002/aenm.201701912.

(18) Clément, R. J.; Bruce, P. G.; Grey, C. P. Review—Manganese-Based P2-Type Transition Metal Oxides as Sodium-Ion Battery Cathode Materials. *J. Electrochem. Soc.* **2015**, *162* (14), A2589. https://doi.org/10.1149/2.0201514jes.

(19) Yabuuchi, N.; Kajiyama, M.; Iwatate, J.; Nishikawa, H.; Hitomi, S.; Okuyama, R.; Usui, R.; Yamada, Y.; Komaba, S. P2-Type $Na_x[Fe_{1/2}Mn_{1/2}]O_2$ Made from Earth-Abundant Elements for Rechargeable Na Batteries. *Nature Mater* **2012**, *11* (6), 512–517. https://doi.org/10.1038/nmat3309.

(20) Niu, Y.; Hu, Z.; Zhang, B.; Xiao, D.; Mao, H.; Zhou, L.; Ding, F.; Liu, Y.; Yang, Y.; Xu, J.; Yin, W.; Zhang, N.; Li, Z.; Yu, X.; Hu, H.; Lu, Y.; Rong, X.; Li, J.; Hu, Y.-S. Earth-Abundant Na-Mg-Fe-Mn-O Cathode with Reversible Hybrid Anionic and Cationic Redox. *Advanced Energy Materials* **2023**, *13* (27), 2300746. https://doi.org/10.1002/aenm.202300746.

(21) Yang, H.; Wang, D.; Liu, Y.; Liu, Y.; Zhong, B.; Song, Y.; Kong, Q.; Wu, Z.; Guo, X. Improvement of Cycle Life for Layered Oxide Cathodes in Sodium-Ion Batteries. *Energy Environ. Sci.* **2024**, *17* (5), 1756–1780. https://doi.org/10.1039/D3EE02934D.

(22) Yabuuchi, N.; Yoshida, H.; Komaba, S. Crystal Structures and Electrode Performance of Alpha-NaFeO2 for Rechargeable Sodium Batteries. *Electrochemistry* **2012**, *80* (10), 716–719. https://doi.org/10.5796/electrochemistry.80.716.

(23) Niu, Y.; Hu, Z.; Zhang, B.; Xiao, D.; Mao, H.; Zhou, L.; Ding, F.; Liu, Y.; Yang, Y.; Xu, J.; Yin, W.; Zhang, N.; Li, Z.; Yu, X.; Hu, H.; Lu, Y.; Rong, X.; Li, J.; Hu, Y.-S. Earth-Abundant Na-Mg-Fe-Mn-O Cathode with Reversible Hybrid Anionic and Cationic Redox. *Advanced Energy Materials* **2023**, *13* (27), 2300746. https://doi.org/10.1002/aenm.202300746.

(24) Billaud, J.; Clément, R. J.; Armstrong, A. R.; Canales-Vázquez, J.; Rozier, P.; Grey, C. P.; Bruce, P. G. β-$NaMnO_2$: A High-Performance Cathode for Sodium-Ion Batteries. *J. Am. Chem. Soc.* **2014**, *136* (49), 17243–17248. https://doi.org/10.1021/ja509704t.

(25) Billaud, J.; Singh, G.; Armstrong, A. R.; Gonzalo, E.; Roddatis, V.; Armand, M.; Rojo, T.; Bruce, P. G. $Na_{0.67}Mn_{1-x}Mg_xO_2$ ($0 \leq x \leq 0.2$): A High Capacity Cathode for Sodium-Ion Batteries. *Energy Environ. Sci.* **2014**, *7* (4), 1387–1391. https://doi.org/10.1039/C4EE00465E.

(26) House, R. A.; Maitra, U.; Jin, L.; Lozano, J. G.; Somerville, J. W.; Rees, N. H.; Naylor, A. J.; Duda, L. C.; Massel, F.; Chadwick, A. V.; Ramos, S.; Pickup, D. M.; McNally, D. E.; Lu, X.; Schmitt, T.; Roberts, M. R.; Bruce, P. G. What Triggers Oxygen Loss in Oxygen Redox Cathode Materials? *Chem. Mater.* **2019**, *31* (9), 3293–3300. https://doi.org/10.1021/acs.chemmater.9b00227.

(27) Jin, T.; Li, H.; Zhu, K.; Wang, P.-F.; Liu, P.; Jiao, L. Polyanion-Type Cathode Materials for Sodium-Ion Batteries. *Chem. Soc. Rev.* **2020**, *49* (8), 2342–2377. https://doi.org/10.1039/C9CS00846B.

(28) Zhu, Y.; Xu, Y.; Liu, Y.; Luo, C.; Wang, C. Comparison of Electrochemical Performances of Olivine $NaFePO_4$ in Sodium-Ion Batteries and Olivine $LiFePO_4$ in Lithium-Ion Batteries. *Nanoscale* **2013**, *5* (2), 780–787. https://doi.org/10.1039/C2NR32758A.

(29) Kim, H.; Shakoor, R. A.; Park, C.; Lim, S. Y.; Kim, J.-S.; Jo, Y. N.; Cho, W.; Miyasaka, K.; Kahraman, R.; Jung, Y.; Choi, J. W. $Na_2FeP_2O_7$ as a Promising Iron-Based Pyrophosphate Cathode for Sodium Rechargeable Batteries: A Combined Experimental and Theoretical Study. *Advanced Functional Materials* **2013**, *23* (9), 1147–1155. https://doi.org/10.1002/adfm.201201589.

(30) Park, C. S.; Kim, H.; Shakoor, R. A.; Yang, E.; Lim, S. Y.; Kahraman, R.; Jung, Y.; Choi, J. W. Anomalous Manganese Activation of a Pyrophosphate Cathode in Sodium Ion Batteries: A Combined Experimental and Theoretical Study. *J. Am. Chem. Soc.* **2013**, *135* (7), 2787–2792. https://doi.org/10.1021/ja312044k.

(31) Barpanda, P.; Oyama, G.; Nishimura, S.; Chung, S.-C.; Yamada, A. A 3.8-V Earth-Abundant Sodium Battery Electrode. *Nat Commun* **2014**, *5* (1), 4358. https://doi.org/10.1038/ncomms5358.

(32) Wang, Y.; Yang, X.; Meng, Y.; Wen, Z.; Han, R.; Hu, X.; Sun, B.; Kang, F.; Li, B.; Zhou, D.; Wang, C.; Wang, G. Fluorine Chemistry in Rechargeable Batteries: Challenges, Progress, and Perspectives. *Chem. Rev.* **2024**, *124* (6), 3494–3589. https://doi.org/10.1021/acs.chemrev.3c00826.

(33) Chen, R.; Ren, S.; Yavuz, M.; Guda, A. A.; Shapovalov, V.; Witter, R.; Fichtner, M.; Hahn, H. Li+ Intercalation in Isostructural Li_2VO_3 and Li_2VO_2F with O^{2-} and Mixed O^{2-}/F^- Anions. *Phys. Chem. Chem. Phys.* **2015**, *17* (26), 17288–17295. https://doi.org/10.1039/C5CP02505B.

(34) Takeda, N.; Hoshino, S.; Xie, L.; Chen, S.; Ikeuchi, I.; Natsui, R.; Nakura, K.; Yabuuchi, N. Reversible Li Storage for Nanosize Cation/Anion-Disordered Rocksalt-Type Oxyfluorides: $LiMoO_2 _{-x} LiF$ ($0 \leq x \leq 2$) Binary System. *Journal of Power Sources* **2017**, *367*, 122–129. https://doi.org/10.1016/j.jpowsour.2017.09.060.

(35) Recham, N.; Chotard, J.-N.; Dupont, L.; Delacourt, C.; Walker, W.; Armand, M.; Tarascon, J.-M. A 3.6 V Lithium-Based Fluorosulphate Insertion Positive Electrode for Lithium-Ion Batteries. *Nature Mater* **2010**, *9* (1), 68–74. https://doi.org/10.1038/nmat2590.

(36) Lee, J.; Papp, J. K.; Clément, R. J.; Sallis, S.; Kwon, D.-H.; Shi, T.; Yang, W.; McCloskey, B. D.; Ceder, G. Mitigating Oxygen Loss to Improve the Cycling Performance of High Capacity Cation-Disordered Cathode Materials. *Nat Commun* **2017**, *8* (1), 981. https://doi.org/10.1038/s41467-017-01115-0.

(37) Clément, R. J.; Kitchaev, D.; Lee, J.; Gerbrand Ceder. Short-Range Order and Unusual Modes of Nickel Redox in a Fluorine-Substituted Disordered Rocksalt Oxide Lithium-Ion Cathode. *Chem. Mater.* **2018**, *30* (19), 6945–6956. https://doi.org/10.1021/acs.chemmater.8b03794.

(38) Barker, J.; Saidi, M. Y.; Swoyer, J. L. A Sodium-Ion Cell Based on the Fluorophosphate Compound $NaVPO_4 F$. *Electrochem. Solid-State Lett.* **2002**, *6* (1), A1. https://doi.org/10.1149/1.1523691.

(39) Serras, P.; Palomares, V.; Goñi, A.; Muro, I. G. de; Kubiak, P.; Lezama, L.; Rojo, T. High Voltage Cathode Materials for Na-Ion Batteries of General Formula $Na_3V_2O_{2x}(PO_4)_2F_{3-2x}$. *J. Mater. Chem.* **2012**, *22* (41), 22301–22308. https://doi.org/10.1039/C2JM35293A.

(40) Tripathi, R.; Wood, S. M.; Islam, M. S.; Nazar, L. F. Na-Ion Mobility in Layered Na_2FePO_4F and Olivine $Na[Fe,Mn]PO4$. *Energy Environ. Sci.* **2013**, *6* (8), 2257–2264. https://doi.org/10.1039/C3EE40914G.

(41) Foley, E. E.; Wong, A.; Vincent, R. C.; Manche, A.; Zaveri, A.; Gonzalez-Correa, E.; Ménard, G.; Clément, R. J. Probing Reaction Processes and Reversibility in Earth-Abundant Na_3FeF_6 for Na-Ion Batteries. *Phys. Chem. Chem. Phys.* **2021**, *23* (36), 20052–20064. https://doi.org/10.1039/D1CP02763H.

(42) Ponrouch, A.; Cabana, J.; Dugas, R.; Slack, J. L.; Palacín, M. R. Electroanalytical Study of the Viability of Conversion Reactions as Energy Storage Mechanisms. *RSC Adv.* **2014**, *4* (68), 35988–35996. https://doi.org/10.1039/C4RA05189K.

(43) Wang, H.; Chen, S.; Fu, C.; Ding, Y.; Liu, G.; Cao, Y.; Chen, Z. Recent Advances in Conversion-Type Electrode Materials for Post Lithium-Ion Batteries. *ACS Materials Lett.* **2021**, *3* (7), 956–977. https://doi.org/10.1021/acsmaterialslett.1c00043.

(44) Lemoine, K.; Hémon-Ribaud, A.; Leblanc, M.; Lhoste, J.; Tarascon, J.-M.; Maisonneuve, V. Fluorinated Materials as Positive Electrodes for Li- and Na-Ion Batteries. *Chem. Rev.* **2022**, *122* (18), 14405–14439. https://doi.org/10.1021/acs.chemrev.2c00247.

(45) Li, H.; Zhou, H. Enhancing the Performances of Li-Ion Batteries by Carbon-Coating: Present and Future. *Chem. Commun.* **2012**, *48* (9), 1201–1217. https://doi.org/10.1039/C1CC14764A.

(46) Fu, W.; Zhao, E.; Sun, Z.; Ren, X.; Magasinski, A.; Yushin, G. Iron Fluoride–Carbon Nanocomposite Nanofibers as Free-Standing Cathodes for High-Energy Lithium Batteries. *Adv Funct Materials* **2018**, *28* (32), 1801711. https://doi.org/10.1002/adfm.201801711.

(47) Entwistle, J.; Ge, R.; Pardikar, K.; Smith, R.; Cumming, D. Carbon Binder Domain Networks and Electrical Conductivity in Lithium-Ion Battery Electrodes: A Critical Review. *Renewable and Sustainable Energy Reviews* **2022**, *166*. https://doi.org/10.1016/j.rser.2022.112624.

(48) Euchner, H.; Clemens, O.; Reddy, M. A. Unlocking the Potential of Weberite-Type Metal Fluorides in Electrochemical Energy Storage. *npj Comput Mater* **2019**, *5* (1), 31. https://doi.org/10.1038/s41524-019-0166-3.

(49) Dey, U. K.; Barman, N.; Ghosh, S.; Sarkar, S.; Peter, S. C.; Senguttuvan, P. Topochemical Bottom-Up Synthesis of 2D- and 3D-Sodium Iron Fluoride Frameworks. *Chem. Mater.* **2019**, *31* (2), 295–299. https://doi.org/10.1021/acs.chemmater.8b04010.

(50) Park, H.; Lee, Y.; Cho, M.; Kang, J.; Ko, W.; Jung, Y. H.; Jeon, T.-Y.; Hong, J.; Kim, H.; Myung, S.-T.; Kim, J. $Na_2Fe_2F_7$: A Fluoride-Based Cathode for High Power and Long Life Na-Ion Batteries. *Energy Environ. Sci.* **2021**, *14* (3), 1469–1479. https://doi.org/10.1039/D0EE02803G.

(51) Foley, E. E., Wu, V. C., Jin, W., Cui, W., Yoshida, E., Manche, A. & Clément, R. J. Polymorphism in Weberite $Na_2Fe_2F_7$ and its Effects on Electrochemical Properties as a Na-Ion Cathode. *Chem. Mater.* **35,** 3614–3627 (2023).

(52) Wang, Y.; Miao, X.; Li, Y.; Park, H.; Lu, Y.; Li, X. Ion-Exchange Enabled New Intercalation Li Metal Fluorides. *Electrochemistry Communications* **2023**, *155*, 107581. https://doi.org/10.1016/j.elecom.2023.107581.

(53) Kang, J.; Ahn, J.; Park, H.; Ko, W.; Lee, Y.; Lee, S.; Lee, S.; Jung, S.; Kim, J. Highly Stable Fe^{2+}/Ti^{3+}-Based Fluoride Cathode Enabling Low-Cost and High-Performance Na-Ion Batteries. *Adv Funct Materials* **2022**, *32* (29), 2201816. https://doi.org/10.1002/adfm.202201816.

(54) Liao, J.; Han, J.; Xu, J.; Du, Y.; Sun, Y.; Duan, L.; Zhou, X. Scalable Synthesis of Na_2MVF_7 (M = Mn, Fe, and Co) as High-Performance Cathode Materials for Sodium-Ion Batteries. *Chem. Commun.* **2021**, *57* (87), 11497–11500. https://doi.org/10.1039/D1CC04449D.

(55) Tressaud, A.; Dance, J.-M.; Portier, J.; Hagenmuller, P. Interactions Magnetiques Dans Les Fluorures de Type Weberite. *Materials Research Bulletin* **1974**, *9* (9), 1219–1226. https://doi.org/10.1016/0025-5408(74)90040-3.

(56) Cosier, R.; Wise, A.; Tressaud, A.; Grannec, J.; Olazcuaga, R.; Portier, J. Sur de Nouveaux Composés Fluorés Ferrimagnétiques à Structure Wébérite. *C. R. Hebd. Seances Acad. Sci. C* **1970**, *271*, 143–145.

(57) Yakubovich, O.; Urusov, V.; Massa, W.; Frenzen, G.; Babel, D. Structure of $Na_2Fe_2F_7$ and Structural Relations in the Family of Weberites $Na_2M^{II}M^{III}F_7$. *Zeitschrift anorg allge chemie* **1993**, *619* (11), 1909–1919. https://doi.org/10.1002/zaac.19936191115.

(58) Badway, F.; Cosandey, F.; Pereira, N.; Amatucci, G. G. Carbon Metal Fluoride Nanocomposites : High-Capacity Reversible Metal Fluoride Conversion Materials as Rechargeable Positive Electrodes for Li Batteries. *J. Electrochem. Soc.* **2003**, *150* (10), A1318. https://doi.org/10.1149/1.1602454.

(59) Lepage, D.; Sobh, F.; Kuss, C.; Liang, G.; Schougaard, S. B. Delithiation Kinetics Study of Carbon Coated and Carbon Free $LiFePO_4$. *Journal of Power Sources* **2014**, *256*, 61–65. https://doi.org/10.1016/j.jpowsour.2013.12.054.

(60) Li, C.; Gu, L.; Tong, J.; Maier, J. Carbon Nanotube Wiring of Electrodes for High-Rate Lithium Batteries Using an Imidazolium-Based Ionic Liquid Precursor as Dispersant and Binder: A Case Study on Iron Fluoride Nanoparticles. *ACS Nano* **2011**, *5* (4), 2930–2938. https://doi.org/10.1021/nn1035608.

(61) Wang, J.; Sun, X. Understanding and Recent Development of Carbon Coating on LiFePO4 Cathode Materials for Lithium-Ion Batteries. *Energy Environ. Sci.* **2012**, *5* (1), 5163–5185. https://doi.org/10.1039/C1EE01263K.

(62) Yabuuchi, N.; Kubota, K.; Aoki, Y.; Komaba, S. Understanding Particle-Size-Dependent Electrochemical Properties of Li_2MnO_3 -Based Positive Electrode Materials for Rechargeable Lithium Batteries. *J. Phys. Chem. C* **2016**, *120* (2), 875–885. https://doi.org/10.1021/acs.jpcc.5b10517.

(63) Furness, J. W.; Kaplan, A. D.; Ning, J.; Perdew, J. P.; Sun, J. Accurate and Numerically Efficient r^2 SCAN Meta-Generalized Gradient Approximation. *J. Phys. Chem. Lett.* **2020**, *11* (19), 8208–8215. https://doi.org/10.1021/acs.jpclett.0c02405.

(64) Tekliye, D. B.; Gautam, G. S. Accuracy of metaGGA Functionals in Describing Transition Metal Fluorides. arXiv January 19, 2024. https://doi.org/10.48550/arXiv.2401.10832. (accessed 07-12-2024).

(65) Martin, A.; Doublet, M.; Kemnitz, E.; Pinna, N. Reversible Sodium and Lithium Insertion in Iron Fluoride Perovskites. *Adv Funct Materials* **2018**, *28* (29), 1802057. https://doi.org/10.1002/adfm.201802057.

(66) Zheng, Y.; Jitto, S.; Hwang, J.; Matsumoto, K.; Hagiwara, R. Multiphase Transformation of NaFeF$_3$ During Desodiation and Sodiation. *ACS Appl. Energy Mater.* **2022**, *5* (11), 14361–14371. https://doi.org/10.1021/acsaem.2c02904.

(67) Van Der Ven, A.; Bhattacharya, J.; Belak, A. A. Understanding Li Diffusion in Li-Intercalation Compounds. *Acc. Chem. Res.* **2013**, *46* (5), 1216–1225. https://doi.org/10.1021/ar200329r.

(68) Coelho, A. A. TOPAS and TOPAS-Academic: An Optimization Program Integrating Computer Algebra and Crystallographic Objects Written in C++. *J Appl Cryst* **2018**, *51* (1), 210–218. https://doi.org/10.1107/S1600576718000183.

(69) Momma, K.; Izumi, F. VESTA 3 for Three-Dimensional Visualization of Crystal, Volumetric and Morphology Data. *J Appl Cryst* **2011**, *44* (6), 1272–1276. https://doi.org/10.1107/S0021889811038970.

(70) Massiot, D.; Fayon, F.; Capron, M.; King, I.; Le Calvé, S.; Alonso, B.; Durand, J.-O.; Bujoli, B.; Gan, Z.; Hoatson, G. Modelling One- and Two-Dimensional Solid-State NMR Spectra. *Magnetic Resonance in Chemistry* **2002**, *40* (1), 70–76. https://doi.org/10.1002/mrc.984.

(71) Prescher, C.; McCammon, C.; Dubrovinsky, L. MossA: A Program for Analyzing Energy-Domain Mössbauer Spectra from Conventional and Synchrotron Sources. *J Appl Cryst* **2012**, *45* (2), 329–331. https://doi.org/10.1107/S0021889812004979.

(72) Kresse, G.; Hafner, J. Ab Initio Molecular Dynamics for Liquid Metals. *Phys. Rev. B* **1993**, *47* (1), 558–561. https://doi.org/10.1103/PhysRevB.47.558.

(73) Kresse, G.; Hafner, J. Ab Initio Molecular-Dynamics Simulation of the Liquid-Metal--Amorphous-Semiconductor Transition in Germanium. *Phys. Rev. B* **1994**, *49* (20), 14251–14269. https://doi.org/10.1103/PhysRevB.49.14251.

(74) Kresse, G.; Furthmüller, J. Efficiency of Ab-Initio Total Energy Calculations for Metals and Semiconductors Using a Plane-Wave Basis Set. *Computational Materials Science* **1996**, *6* (1), 15–50. https://doi.org/10.1016/0927-0256(96)00008-0.

(75) Kresse, G.; Furthmüller, J. Efficient Iterative Schemes for Ab Initio Total-Energy Calculations Using a Plane-Wave Basis Set. *Phys. Rev. B* **1996**, *54* (16), 11169–11186. https://doi.org/10.1103/PhysRevB.54.11169.

(76) Blöchl, P. E. Projector Augmented-Wave Method. *Phys. Rev. B* **1994**, *50* (24), 17953–17979. https://doi.org/10.1103/PhysRevB.50.17953.

(77) Kresse, G.; Joubert, D. From Ultrasoft Pseudopotentials to the Projector Augmented-Wave Method. *Phys. Rev. B* **1999**, *59* (3), 1758–1775. https://doi.org/10.1103/PhysRevB.59.1758.

(78) Sun, J.; Ruzsinszky, A.; Perdew, J. P. Strongly Constrained and Appropriately Normed Semilocal Density Functional. *Phys. Rev. Lett.* **2015**, *115* (3), 036402. https://doi.org/10.1103/PhysRevLett.115.036402.

(79) Anisimov, V. I.; Aryasetiawan, F.; Lichtenstein, A. I. First-Principles Calculations of the Electronic Structure and Spectra of Strongly Correlated Systems: The LDA+ U Method. *J. Phys.: Condens. Matter* **1997**, *9* (4), 767. https://doi.org/10.1088/0953-8984/9/4/002.

(80) Sai Gautam, G.; Carter, E. A. Evaluating Transition Metal Oxides within DFT-SCAN and SCAN + U Frameworks for Solar Thermochemical Applications. *Phys. Rev. Materials* **2018**, *2* (9), 095401. https://doi.org/10.1103/PhysRevMaterials.2.095401.

(81) Long, O. Y.; Sai Gautam, G.; Carter, E. A. Evaluating Optimal *U* for *3d* Transition-Metal Oxides within the SCAN+*U* Framework. *Phys. Rev. Mater.* **2020**, *4* (4), 045401. https://doi.org/10.1103/PhysRevMaterials.4.045401.

(82) Perdew, J. P.; Burke, K.; Ernzerhof, M. Generalized Gradient Approximation Made Simple. *Phys. Rev. Lett.* **1996**, *77* (18), 3865–3868. https://doi.org/10.1103/PhysRevLett.77.3865.

(83) Jain, A.; Hautier, G.; Ong, S. P.; Moore, C. J.; Fischer, C. C.; Persson, K. A.; Ceder, G. Formation Enthalpies by Mixing GGA and GGA + U Calculations. *Phys. Rev. B* **2011**, *84* (4), 045115. https://doi.org/10.1103/PhysRevB.84.045115.

(84) Wang, L.; Maxisch, T.; Ceder, G. Oxidation Energies of Transition Metal Oxides within the GGA + U Framework. *Phys. Rev. B* **2006**, *73* (19), 195107. https://doi.org/10.1103/PhysRevB.73.195107.

(85) Ong, S. P.; Richards, W. D.; Jain, A.; Hautier, G.; Kocher, M.; Cholia, S.; Gunter, D.; Chevrier, V. L.; Persson, K. A.; Ceder, G. Python Materials Genomics (Pymatgen): A Robust, Open-Source Python Library for Materials Analysis. *Computational Materials Science* **2013**, *68*, 314–319. https://doi.org/10.1016/j.commatsci.2012.10.028.

(86) McDermott, M. J.; Dwaraknath, S. S.; Persson, K. A. A Graph-Based Network for Predicting Chemical Reaction Pathways in Solid-State Materials Synthesis. *Nat Commun* **2021**, *12* (1), 3097. https://doi.org/10.1038/s41467-021-23339-x.

Mg substitution impacts stability and electrochemical properties of the weberite $Na_2Fe_2F_7$ cathode